Effects of Electrode Mass-loading on the Electrochemical Properties of Porous MnO$_2$ for Electrochemical Supercapacitor

Chuanyun Wan[*]*, Liyang Yuan, Haiyan Shen*

School of Chemical and Enviormental Engineering, Shanghai Institute of Technology, Shanghai 200235, China
[*]E-mail: cywan@sit.edu.cn

Porous MnO$_2$ nanostructure with large surface area and large pore volume was prepared by a facial chemical method in large scale. The physical properties of the as-prepared MnO$_2$ were characterized by X-ray diffraction (XRD) analysis, Brunauer-Emmett-Teller (BET) method and scanning electron microscope (SEM). The effect of electrode mass-loading on the electrochemical properties of MnO$_2$ electrodes was studied by cyclic voltammetry (CV), impedance spectrum test and chronopotentiometry methods in 1.0M Na$_2$SO$_4$ solution. The results showed that the as-prepared MnO$_2$ exhibited ideal capacitive behavior in a voltage window of 0~1.0V. With increasing of MnO$_2$ mass from 5 to 25 mg cm^{-2} in electrode, the specific capacitance calculated from the CV curves at 2mV s^{-1} decreased from 452 to 205 F g^{-1}. Impedance spectrum tests indicated that the reduction of specific capacitance was mainly due to the increase of charge transfer resistance and the slow ion diffusion in the thicker electrode. Ragone plots indicated that the MnO$_2$ electrode with 5mg cm^{-2} mass-loading possessed good power-energy density characteristics. An energy density of 26.6Wh Kg^{-1} still remained 24Wh Kg^{-1} when the power density increased from 50 W Kg^{-1} to 5 KW Kg^{-1}. These results indicated that porous MnO$_2$ and thinner mass loading is benefit for applications in electrochemical supercapacitor.

1. INTRODUCTION

Electrochemical supercapacitors are currently under development for applications as alternative energy storage devices due to their higher specific power and long cycle life compared with rechargeable batteries and higher specific energy compared with conventional capacitors[1,2]. Considerable efforts have been focused on the development of advanced electrode materials. Up to now, three main categories of active electrode materials, carbon[3-5], conducting polymer[6,7] and transition metal oxide[8-12], have been used in supercapacitors. Among them, transition metal oxide,

eg. $RuO_2 \cdot xH_2O$, shows great performance as an electrode material for pseudocapacitors. However, the high cost and toxicity of hydrous ruthenium oxide hinders its wide application[1,3]. Recently, manganese dioxides has been considered as a promising electrode for electrochemical capacitor and is currently attracting a lot of interest due to its low cost, low toxicity and excellent electrochemical performance[12-28].

According to the charging mechanism of manganese dioxide, the following reaction on MnO_2 electrode will occur[13,20]

$$MnO_2 + A + e^{-1} \leftrightarrow MnOOA \qquad\qquad (1)$$

Where A =Li^+, Na^+, K^+, H^+. The first charging mechanism is based on the concept of H^+ or alkali metal cations such as Na^+ ions in the electrochemical reduction and deintercalation upon oxidation. The secondary one is based on the surface adsorption of electrolyte cations. In one word, Eq.(1) indicates that high ionic and electronic conductivity and the large surface area of the electrode material are necessary in order to utilize the theoretical specific capacitance($\sim$1000F g^{-1}) of MnO_2 [21]. In fact, in order to develop an advanced EC device, current efforts are being focused on the improvement of the capacity performance of MnO_2 and many manganese dioxides with various structures and morphologies have been fabricated via chemical and electrochemical routes[14-18]. The main research results indicated that the specific capacitance and power-energy density performance of manganese dioxide are not only related to its crystal structure and surface properties but also greatly related to its textural properties including morphology, surface area, pore volume and pore dimension[14-18,22-26]. Much work has been done on increasing the surface area of manganese dioxide to improve its electrochemical performance. For example, Yu et al[27] synthesized manganese dioxide by co-precipitation in the presence of Pluronic P123 surfactant and obtained nanostructure manganese dioxide with a highest specific area of ca.270m^2 g^{-1} and a maximal specific capacitance of 176F g^{-1} at 2mA cm^{-2}. Liu et al[16] used SiO_2 spheres as template and prepared MnO_2 with a large surface area by a template–assisted hydrothermal process. Hollow manganese dioxide with a specific surface area of 253m^2 g^{-1} was obtained and exhibited an initial capacitance of 299F g^{-1} in potential cycling tests at 5mV s^{-1}. It is obvious that active material with large specific area is beneficial to manganese dioxide for supercapacitor. However, the addition of surfactant evidently increases the cost and the application of template will make the synthesis route complicated.

In our previous work, we have successfully synthesized manganese oxide with large specific surface area through simple redox reaction between Mn^{2+} and MnO_4^- and proved that this method was a simple method to obtain porous MnO_2 for electrochemical supercapacitor[28]. Here, we synthesized porous MnO_2 sample in large scale and studied the electrochemical performance of manganese oxide with large specific surface and discussed the effect of electrode mass on electrochemical performance in detail. Considering the present electrode mass-loading in literature[12,18], two types of mass-loading with ca. 5mg cm^{-2} and ca. 25mg cm^{-2} were exemplified as the thin electrode and thick electrode, respectively, to investigate the effect of mass-loading/thickness of electrode on electrochemical of MnO_2.

2. EXPERIMENTAL

Chemical grade manganese acetate ($Mn(CH_3COO)_2 \cdot 4H_2O$) and potassium permanganate ($KMnO_4$) were used as starting materials. The concentrations of $Mn(CH_3COO)_2$ and $KMnO_4$ were 0.15M and 0.1M, respectively. Porous MnO_2 particles were synthesized by redox reaction in aqueous medium, 5 L of 0.1M $KMnO_4$ solution was slowly bumped into 5 L of 0.15M $Mn(CH_3COO)_2$ solution and stirred continuously for 10 h. A dark-brown precipitate thus formed. It was washed for several times with double distilled water, centrifuged, and dried at 110^0C for 12h.

Powder X-ray diffraction patterns of MnO_2 were recorded using Rigaku 2200X diffractometer with Cu Kα radiation (λ=1.54Å) as the source. The microstructure of the MnO_2 particles was examined using an FIRS Quanta200 scanning electron microscope. The Brunauer-Emmett-Teller surface area and pore volume were measured by the nitrogen gas adsorption-desorption method at 77K using an ASAP 220 Quantachrome surface area analyzer. The pore size distribution was calculated by the Barrett-Jayner-Halenda(BJH) method using the desorption branch of the isotherm.

Working electrodes for electrochemical measurements were prepared on Nickel foam. Active material MnO_2(65% by weight), super-P carbon(25% by weight) and polytetrafluoroethylene (PTFE)(10% by weight) were ground in a mortar and a few drops of ethanol was added to mix well. The mixture was pressed onto nickel foam to fabricate two types of working electrodes with ca. 5mg cm^{-2}(denoted as J5) and ca. 25mg cm^{-2}(denoted as J25) of MnO_2 mass loading, respectively. Both electrodes were dried at 50^0C under vacuum for 12h before analysis. The test cell consisted of a MnO_2 working electrode, a Pt counter electrode and an SCE(saturated calomel electrode) reference electrode, and 1M sodium sulfate solution was used as the electrolyte. Electrochemical studies were carried out using an Autolab electrochemical workstation.

3. RESULTS AND DISCUSSION

The morphology and crystalline structure of the as-prepared MnO_2 are shown in Fig.1. It can be seen clearly that the prepared MnO_2 are composed of uniformly distributed spherical aggregates of 50-100nm nanoparticles with clear interparticle boundaries. Such a nanostructure could be expected to shorten significantly the distance of ions diffusion in solid phase and exhibit good pseudocapacitance[26]. The XRD diffraction pattern of MnO_2 exhibits weak and broad peaks distinguishable around 2θ=24.0, 37.7 and 66^0. These peaks are difficult to be indexed to a certain crystallographic form. Even so, it does indicate that the formed MnO_2 is in poorly crystalline phase and is a mixture of poorly crystallized oxides and amorphous oxide[25].

Fig.2 is the nitrogen adsorption-desorption isotherms of the as-prepared MnO_2. The as-prepared MnO_2 exhibits a hysteresis loop in the relative pressure(P/P_0) range of 0.6 to ~1. This hysteresis loop might be ascribed to the presence of mesoporous structure and microstructure in MnO_2 nanoparticles. The BJH pore-size distribution(the inset in Fig.2) clearly exhibit many mesopores and micropores in as-prepared MnO_2. According to the nitrogen adsorption-desorption isotherms of the as-prepared MnO_2, the BET surface area is calculated to be 292.5m^2 g^{-1} and the pore volume is calculated to be

$0.67cm^3$ g^{-1}. The high special BET surface area and large amount of pore structure provide the possibility of efficient transport of electrons and ions, which leads to the high electrochemical capacity of MnO_2.
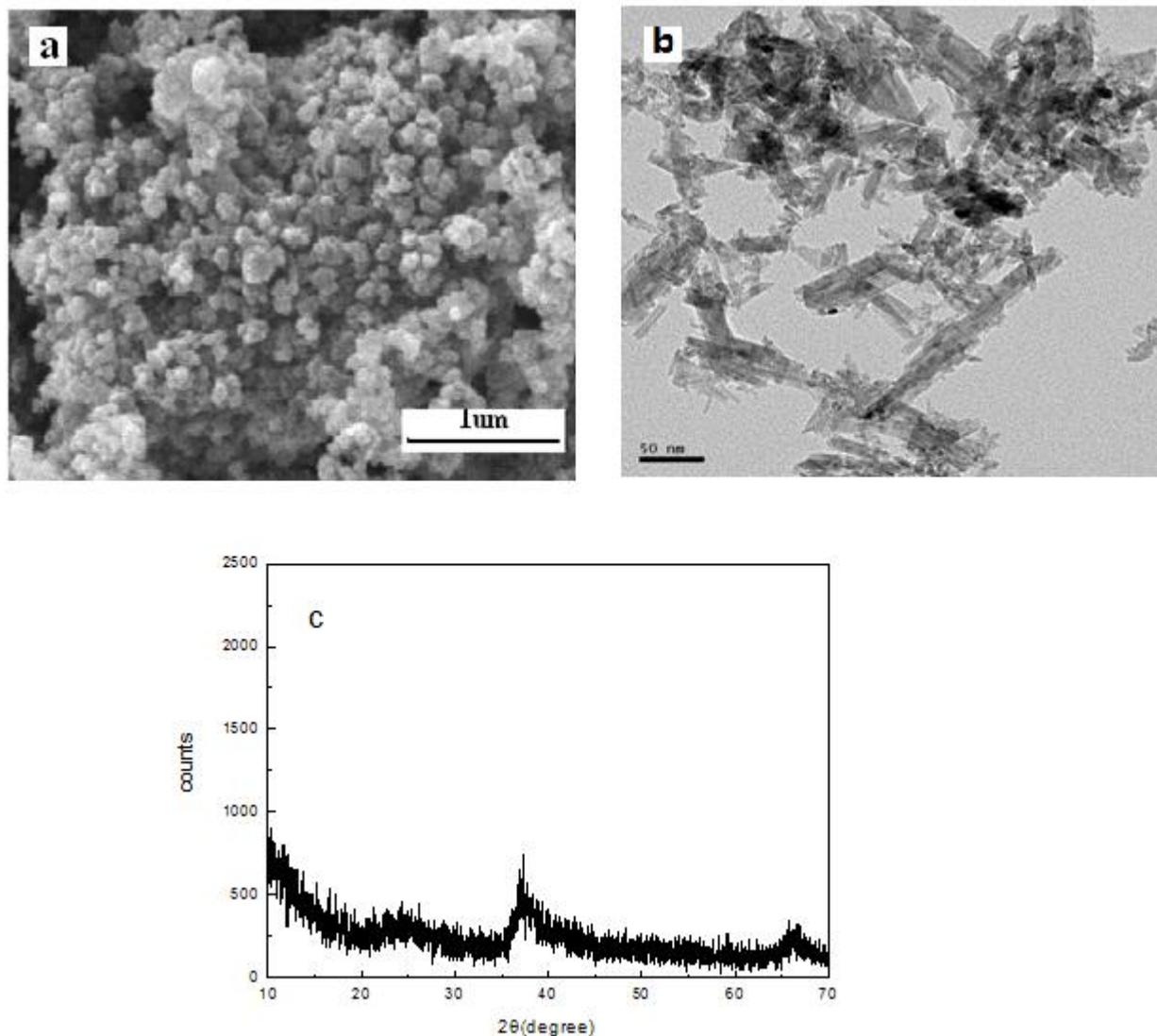
Figure 1. SEM image(a), TEM image(b) and XRD pattern(c) of the as-prepared MnO_2

Cyclic voltammetry (CV) has been considered to be a suitable experimental technique for evaluating the electrochemical capacitive properties of active material[1,12,28]. Here, cyclic voltammetry in the potential range between 0 and 1.0V (versus SCE) was applied to evaluate the electrochemical properties of the MnO_2 electrode in 1M Na_2SO_4 neutral solution. In order to evaluate the electrochemical properties of the as-prepared MnO_2 more clearly, the electrodes with different MnO_2 loading are applied to investigate. Fig.3 a and b show the CV curves of the electrode J5 and the electrode J25 measured at various scan rates in 1M Na_2SO_4 solution, respectively. It can be clearly seen that all voltammograms are nearly perfect rectangular in shape, revealing the perfect electrochemical capacitive behavior of the synthesized MnO_2 [1]. All the curves of the electrode J5 and J25 show no peaks, indicating that both electrodes are charged and discharged at a pseudoconstant

rate over the complete voltammetric cycle and the surface process, that is, the adsorption/desorption of alkali cation, occurs in the as-prepared MnO_2, which is likely predominant in amorphous MnO_2[21,24]. By contrast, an obvious distortion from the rectangular shape in the CV curves for electrode J25 occurs (Fig.3b). This phenomenon can be explained from the view of the ionic motion in electrolyte to MnO_2 solid phase. It is evident that the thickness of the electrode J5 is much thinner than that of the electrode J25. Hence, it can be speculate that a longer distance of ionic motion in the electrode J25 is necessary from electrolyte to the inner MnO_2. In the range of the applied scan rates, alkali cations have enough time to reach the surface of MnO_2 for the electrode J5 for its thin thickness. The absorption/desorption reaction can occur favorably.
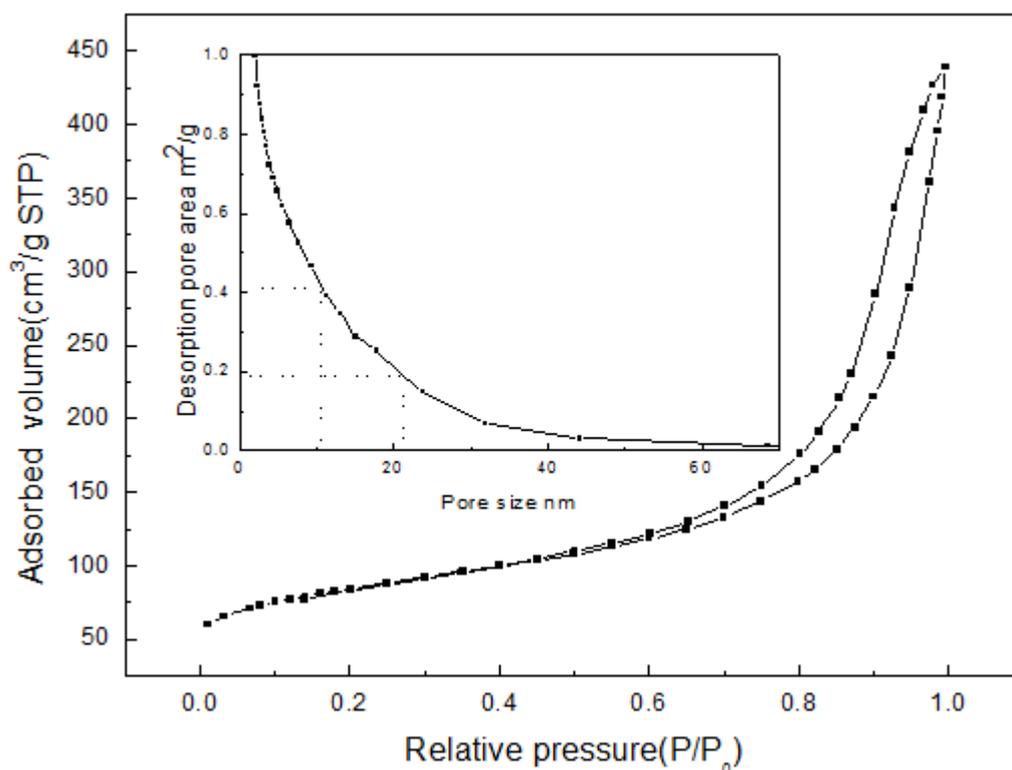
Figure 2. Nitrogen adsorption-desorption isotherms of the as-prepared MnO_2. The inset shows relative pore area distributions.

Hence, there is no obvious deviation from rectangularity of the CV.This electrode presents a specific capacitance of 452F g^{-1} at 2mV s^{-1}. As for the electrode 25, the diffusion of ions from electrolyte can gain access to almost all available pores of the electrode at low scan rates, leading to a complete insertion reaction, and therefore, it shows almost ideal capacitive behavior. With the increase of scan rates, some alkali cations don't have enough time to absorb on the MnO_2 surface due to the polarization of the diffusion and desolvation of alkali cation, and consequently the adsorption on the MnO_2 surface is incomplete and the potential jump at lower and higher ends delays. The deviation from rectangularity of the CV becomes obvious. Even so, there is no doubt that the as-prepared porous MnO_2 has a good pseudocapacitive behavior.
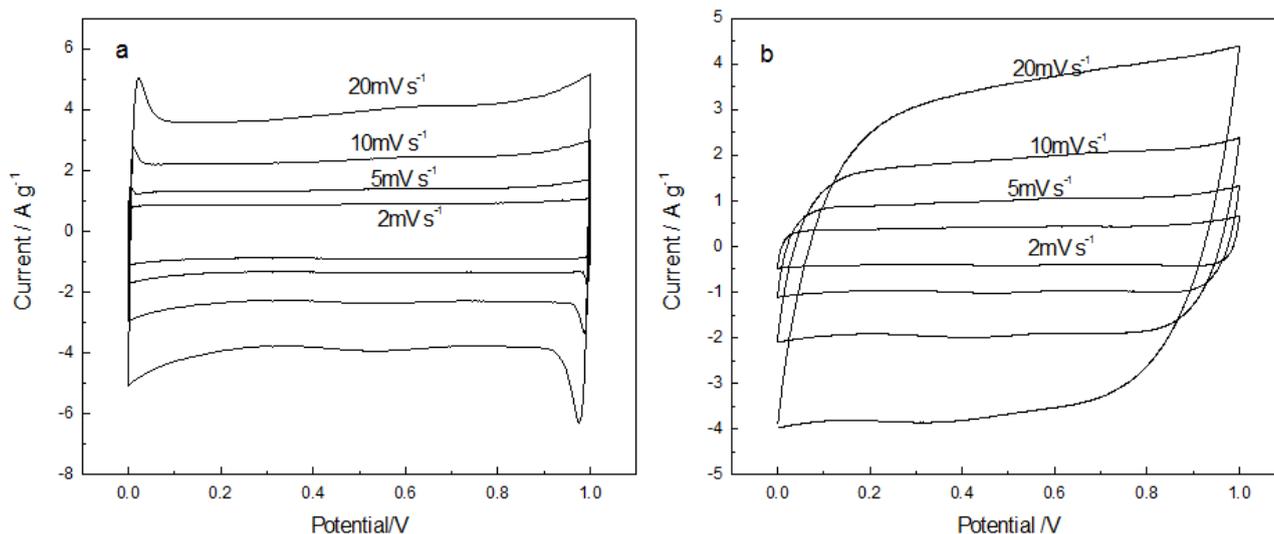
Figure 3. Cyclic voltammogram curves of the Electrode J5(a) and J25(b) measured at various scan rates in 1M Na_2SO_4 solution.
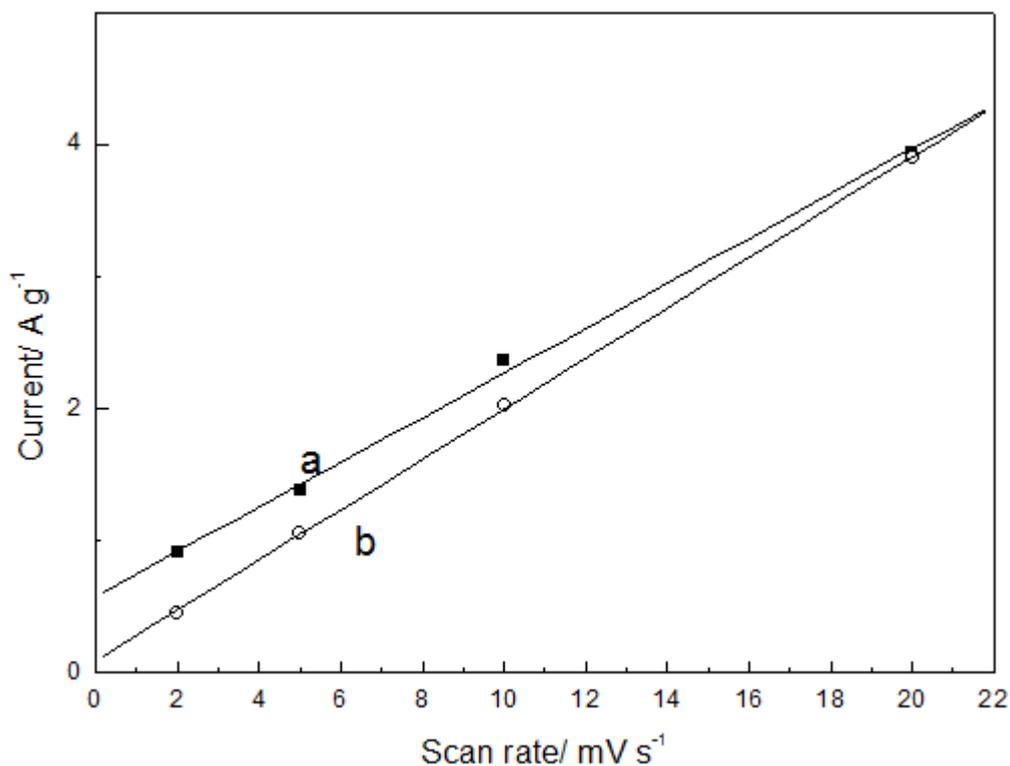
Figure 4. Plots of cathodic current change of the electrode J5(a) and J25(b) vs. scan rates. Currents were measured at the middle of the plateau at 0.5V/ Ref.

Fig.4 shows the plot of specific cathodic current change (i.e. the current value measured at the middle of the plateau at 0.5V in the CVs) with scan rate. It can be seen that the cathodic currents in the electrode J25 at lower scan rates (<20mV s^{-1}) are clearly lower than that in the electrode J5. There is a perfect linear relationship between cathodic current and scan rate and a deviation of current from zero point. This linear relationship characterization of current with scan rate and the deviation of current

from zero point exhibits that the currents measured from the CV experiments consist of purely capacitive current and pseudocapacitive current. With reduction of the thickness of the electrode, the current response increases, indicating that the utilization of MnO_2 were more efficient in the thinner electrode (J5) than in the thicker electrode(J25).

According to the measured CV curves, the specific capacitance can be calculated using half the integrated area of the CV curve to obtain the charge (Q) and subsequently dividing the charge by the mass of the electrode (m) and width of the potential window (ΔV). This equation is

$$C=Q/m\,(\Delta V) \qquad (1)$$

On the other hand, according to the definition of pseudocapacitance, the specific capacitance of MnO_2 can also be calculated by the formula:

$$C_\phi = i/v \qquad (2)$$

Where C_ϕ is the differential capacitance, i is the current density, v is the scan rate.

Fig.5 shows the dependence of the specific capacitance on electrode film mass, for various scan rates. According to equation (1), at a scan rate of 2mV s^{-1}, maximum specific capacitances of 454F g^{-1} and 205F g^{-1} were obtained for the electrode J5 and J25, respectively while their values changed to 452F g^{-1} and 224F g^{-1}, respectively, when equation (2) was used. With increasing of electrode mass, the specific capacitance of MnO_2 decreases. The difference of the electrode J5 and J25 in the capacitance behavior is associated the thickness of MnO_2 film in the electrode J5 and J25.
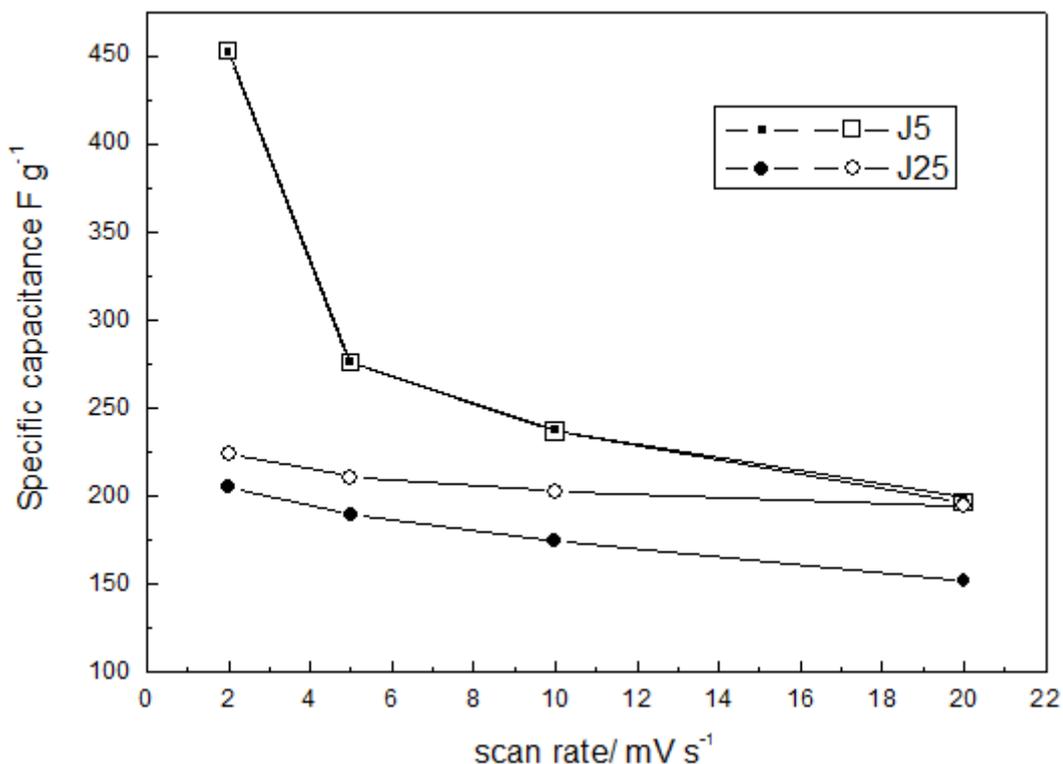
Figure 5. Specific capacitance of the electrode J5 and J25 as a function of scan rate. Filled symbols are calculated using equation (1) and open one using equation (2).

For lower MnO_2 mass, the thickness of the electrode J5 is much thinner than that of the electrode J25, which vacillate electrolyte penetration into the electrode and alkali cations diffusion to inner pores in MnO_2 nanostructure. For the electrode J5, the difference of specific capacitance value from equation (1) and from equation (2) is almost zero, indicating that the ions diffusion in porous MnO_2 is not dominant at the voltage range considered, proved by the ideal mirror-image of CV curves in Fig.3a. For the electrode J25, the specific capacitance value calculated by the equation (1) is much lower than that from the equation (2), indicating that there is an obvious resistance in the electrode J25. Therefore, there is a deviation from rectangularity of the CVs (shown in Fig.3b). With increasing of the scan rates, the specific capacitance decreases. This result has been commonly observed by others [26, 29, 30]. It can be explained from the charge storage mechanism. As for MnO_2, the charge storage might only involve the surface atoms of MnO_2, i.e. the capacitance of MnO_2 results from its surface reaction. Hence, the pseudocapacitance is critically dependent on the effective surface area which is associated with pore distribution and particle size. As for one kind of MnO_2 sample, the pseudocapacitance obtained is critically dependent on the condition of prepared electrode (e.g. electrode mass, electrode porosity, conductivity, and etc.), which greatly effect the effective surface area which is proportion to the available redox reaction active sites. Compared the specific capacitance of the electrode J5 and J25, it can be concluded that the effective surface area is apparently different. The number of available redox reaction active sites in the electrode J5 is much larger than that in the electrode J25 at scan rates considered. Meanwhile, the change of the available redox reaction active sites in the electrode J5 with scan rates is much quicker than that in the electrode J25. In order to illustrate this difference, the available redox reaction active sites per mole (Z) from the specific capacitance can be calculated according to the following relation [31]

$$Z=C \ (\Delta V) \ M/F \qquad\qquad (3)$$

Where C is specific capacitance calculated from equation (1), ΔV is the potential window, M is the molecular weight of MnO_2 and F is the Faraday constant (96500C mol^{-1}).

Fig.6 is a plot of the calculated active sites of MnO_2 against scan rates. The number of redox reaction sites decreased from 0.41 to 0.18 at the scan rate of 2mV s^{-1} when the electrode mass increased from 5mg cm^{-2} to 25mg cm^{-2}. When the scan rate increased to 20mV s^{-1}, the number of redox reaction sites for the electrode J5 and J25 decreased to 0.18 and 0.14, respectively. The change difference of redox reaction active sites in Electrode J5 and J25 with scan rates is associated with the depth of ions diffusion in MnO_2 pores. For the electrode J5, the pore size which the cation ions can accessible at 2mV s^{-1} is ca.10nm, which is much smaller that that in the electrode J25 ca.22nm. With increasing of scan rates, the small pore size will restrain the movement of cation ions into material, resulting in a high reduction of pseudocapacitance.

To better understand the electrochemical properties of the electrodes with different MnO_2 mass, electrochemical impedance spectroscopy over the frequency range of $10^5 \sim 10^{-2}$ Hz was measured. Fig.7A shows the Nyquist plots obtained for the electrode J5 and J25. It can be seen that the Nyquist plots of the electrode J5 and J25 both consist of a semicircle at midhigh frequency and a linear region at low frequency. Such a pattern of the EIS can be fitted by an equivalent circuit shown in the inset of Fig.7A. For both electrode J5 and J25, the intercept at real axis $Z^{'}$ is almost the same (~0.18Ω), which means that the electrodes with different MnO_2 mass have almost the same equivalent series

resistance(ESR) value(including ionic resistance of electrolyte, intrinsic resistance of active materials, and contact resistance at the active material/current interface)[32]. That is to say, the increase of electrode mass here didn't increase the ESR value greatly. Therefore, ESR is not the key factor to affect the pseudocapacitance when scan rates increase.
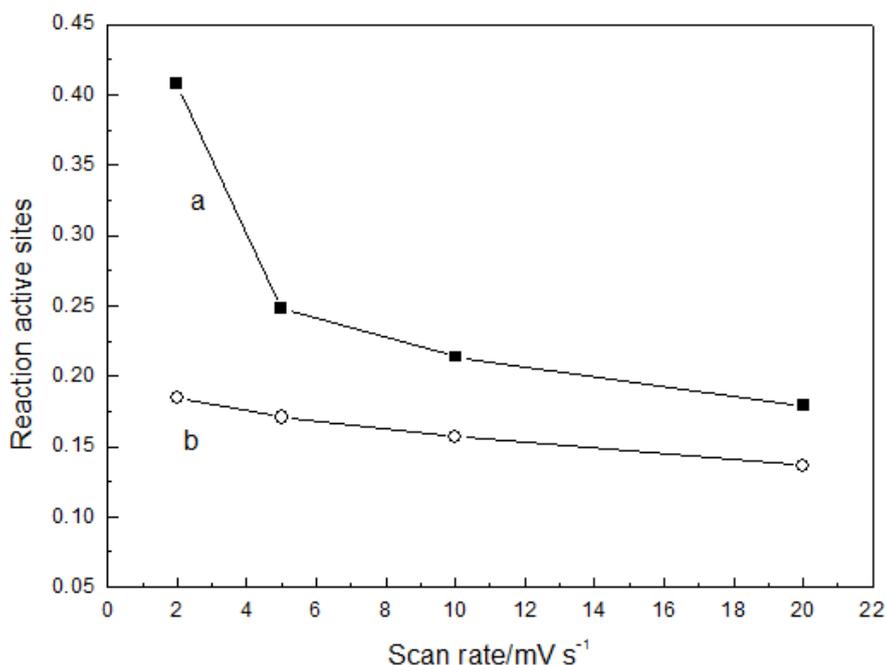
Figure 6. Reaction active sites of the as-prepared MnO$_2$ in the electrode J5(a) and J25 (b) vs. scan rates
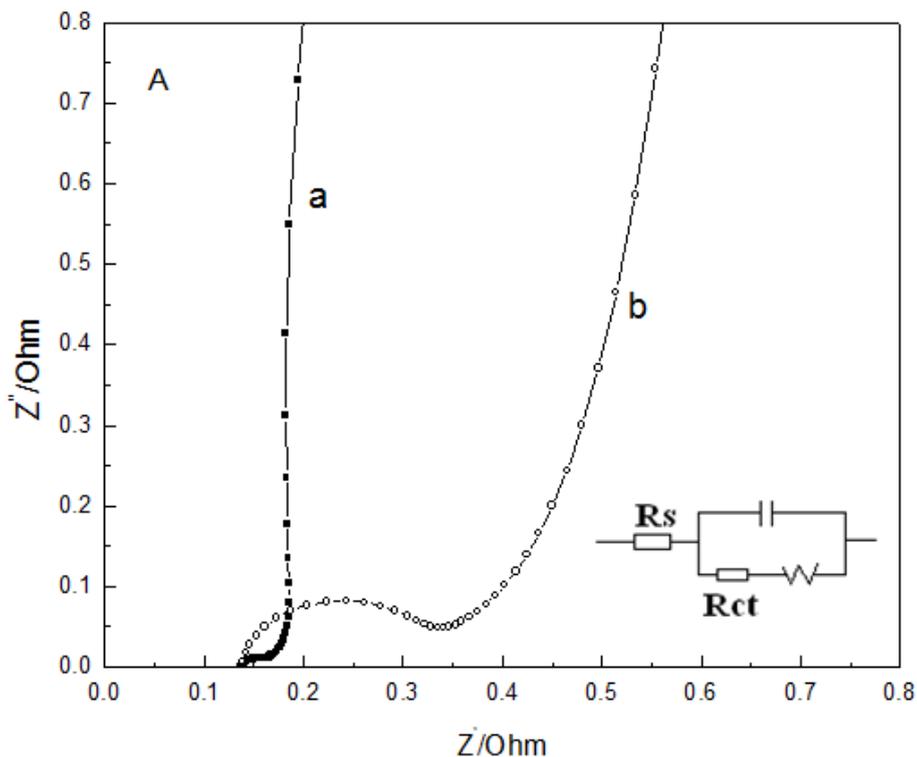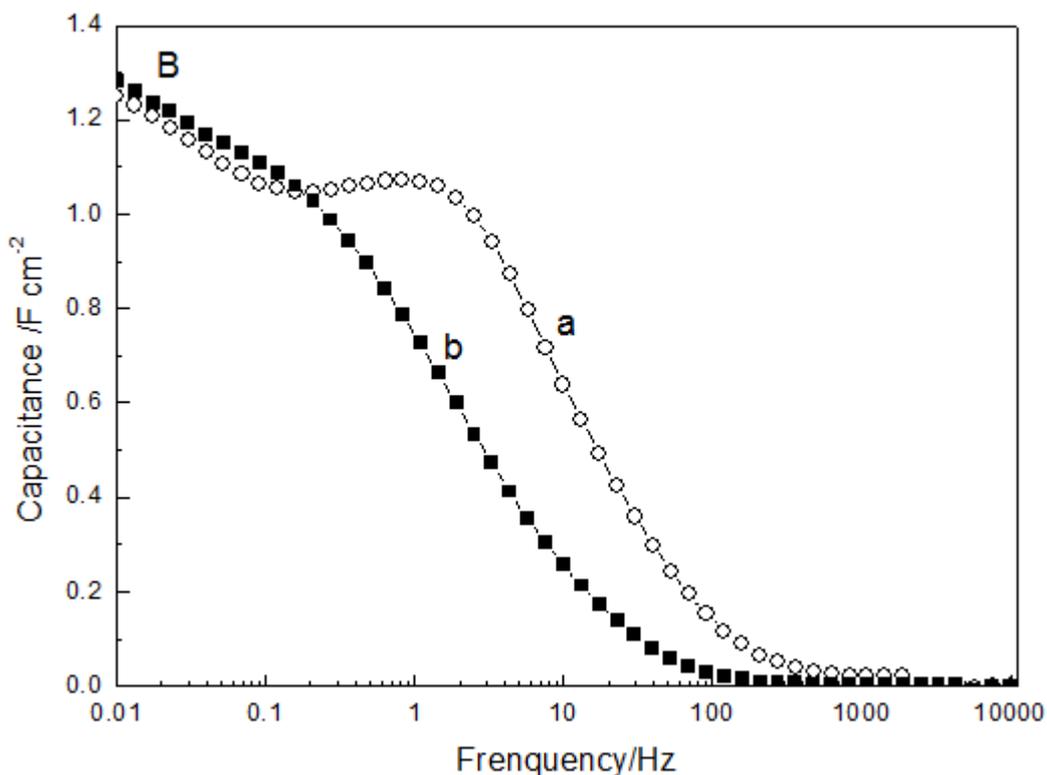
Figure 7. Electrochemical impedance spectra(A) and frequency dependence of capacitance (B) of the electrode J5(a) and J25(b). The inset of (A) is the equivalent circuit)

The semicircle at midhigh frequency region is associated with the charge transfer (R_{ct}) processes occurring at the electrode/electrolyte interface, and double layer capacitance [33]. The diameter of the semicircle of the electrode J5 is much lower than that of the electrode J25, which means that the R_{ct} of the electrode J25 is much larger than that of the electrode J5. This can be explained why a lower pseudocapacitance was obtained for the electrode25 at the same scan rates. The linear regions at low frequency are attributed to both Warburg impedance (diffusion of cation ions in MnO_2 particle and the electrolyte in electrode pores) and insertion capacitance (accumulation of cation ions on MnO_2 surface) [34]. The linear region at low frequency for the electrode J5 comes closer to an ideal straight line along the imaginary axis($Z^{''}$), which indicates that the MnO_2 material in the electrode J5 has low diffusion resistance and cation ions can more easily penetrate into the pores of the material.

For the electrode J25, the linear region of plots exhibit that an angle of about 75^0 relative to the real axis, indicating that the electrode process is not perfectly capacitive in nature and is also under diffusion control. The frequency dependence of capacitance for both electrodes can be presented by transforming the experimental impedance data, $Z^{''}(f)$, to capacitance, $C(f)$, according to the equation $Z^{''} = (2\pi fC)^{-1}$[32, 35].
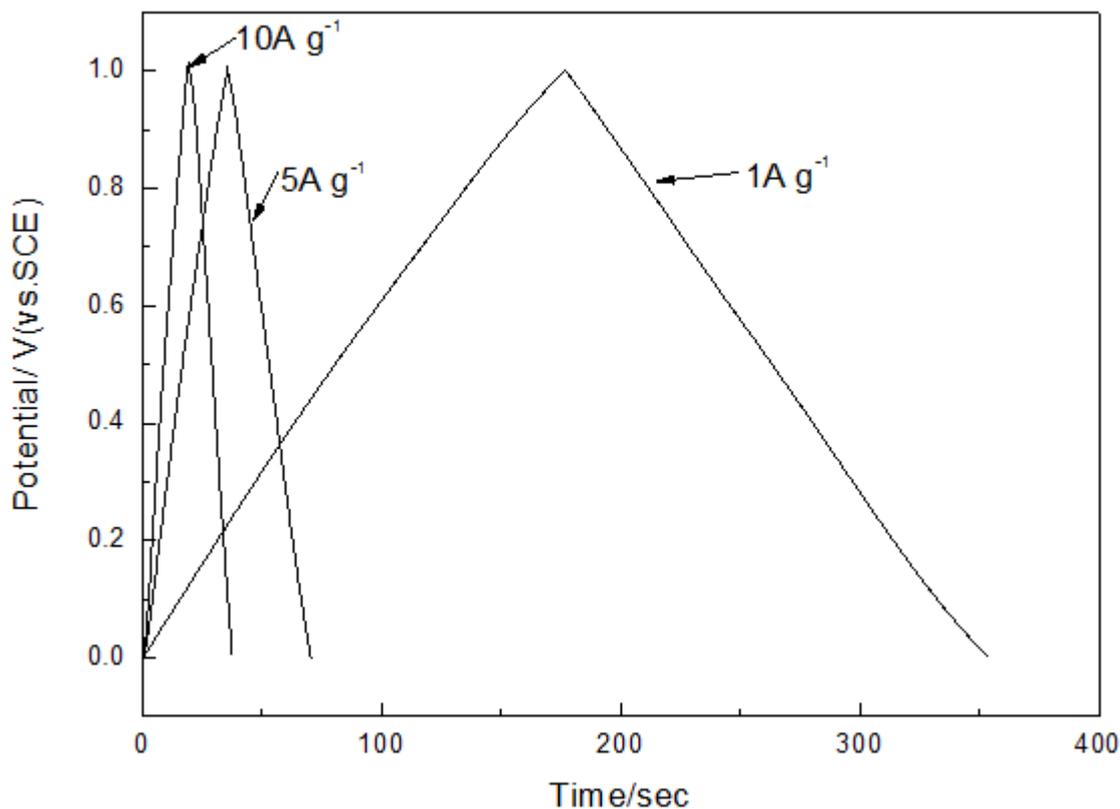
Figure 8. Charge/discharge curves of the electrode J5 measured at different current densities in 1M Na$_2$SO$_4$ between 0 and 1.0V vs. SCE.

As shown in Fig.7B, the electrode J5 has a larger capacitance in the frequency range of 0.2-2000Hz, although the capacitance for both electrodes were almost the same at the frequency low enough (e.g. <0.01Hz). For electrode J5, charge saturation occurred at about 2Hz, indicating that the thickness of the diffusion layer, $\delta = (\pi DT)^{1/2}$(t: relaxation time) can easy to reach the center of the particle. As we know, a negative factor in application of manganese dioxide for electrochemical capacitor is its low electronic and ionic conductivity. A thin manganese dioxide films (~1μg cm^{-2}) have been obtained and exhibited ideal capacitive behavior in a voltage window of 0-0.9V and showed a specific capacitance of ~700F g^{-1}[36]. Hence, decreasing of the manganese dioxide film mass is important for the access of the cation ions to the manganese dioxide surface and to utilize the active material.

To extensively characterize the electrochemical properties of the electrode J5 the charge-discharge behavior was examined by chronopotentiametry. Fig.8 shows the charge/discharge curves of the electrode J5 measured at different charge/discharge current densities. The charge/discharge curves are almost linear and the charge curves are very symmetric to their corresponding discharge counterparts in the whole potential region, indicating that the electrode has a good capacitive behavior. The charge-discharge characterization for the electrode J35 is very similar to the electrode J5. The specific capacitance values were calculated from charge-discharge curves using the following equation [25]

$$SC = It/ (\Delta Vm) \qquad\qquad (4)$$

Where I is the discharge (or charge current), t is the discharge (or charge) time, ΔV (=1.0V) is the potential window of cycling, and m is the mass of MnO_2. The discharge SC values and charge-discharge efficiency for the electrode J5 and J25 are presented in Fig.9. It is obvious that the discharge SC values for the electrode J5 is larger than that for electrode 25. At 0.1A g^{-1}, the SC value for the electrode J5 is ca.192F g^{-1} while the SC value for the electrode J25 is less than 140F g^{-1}. With increasing of current density, the reduction of SC for the electrode 25 is much quicker than the electrode J5.
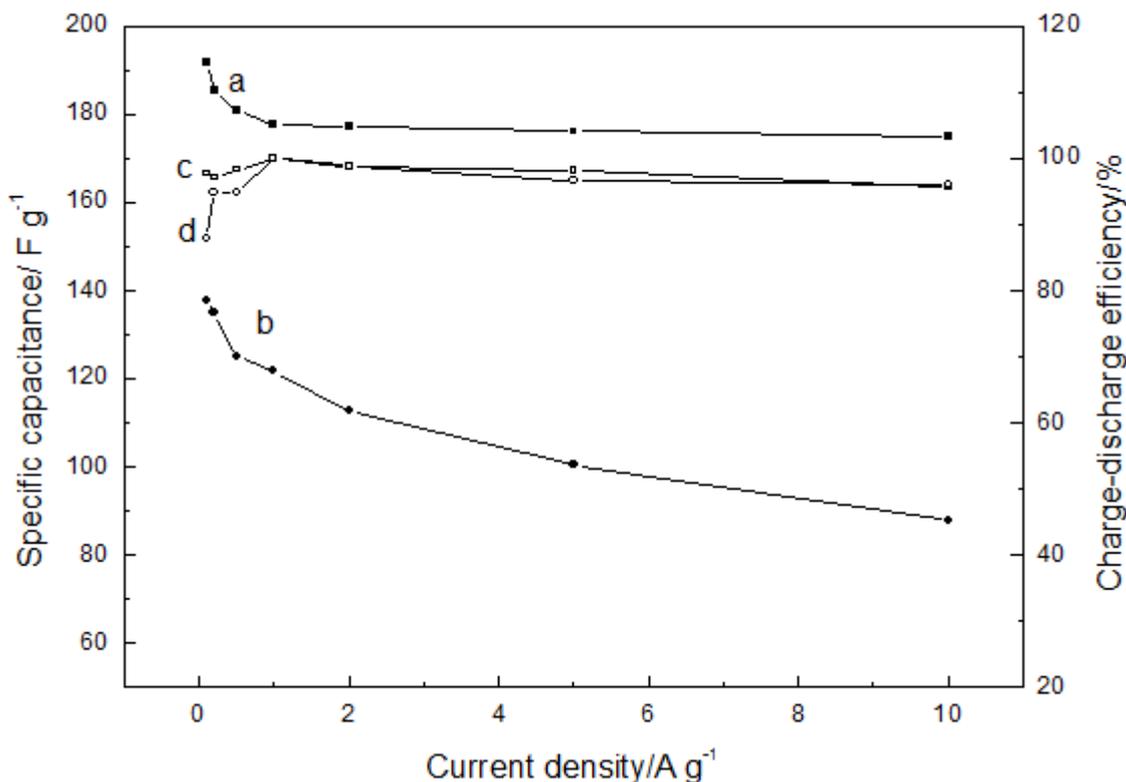
Figure 9. Dependence of specific capacitance (a,b) and charge-discharge efficiency(c,d) on current density of charge-discharge cycling of the electrode J5(a,c) and J25(b,d) in 1M Na_2SO_4 between 0 and 1.0 vs. SCE)

The charge-discharge efficiency of the electrode J5 is little lower than that of the electrode J25 although they both are close to 100%. This difference is due to the larger electrochemical resistance and low ions diffusion in manganese dioxide phase (see Fig.7A).

Fig.10 show the Ragone plots of the electrode J5 and J2. The energy (E) and power (P) of MnO_2 in the electrode J5 and J25 were calculated from their respective charge-discharge curves using the following equations [3, 29]

$$E = \frac{1}{2} C \, (\Delta V)^2 \qquad\qquad (5)$$

$$P = I \, (\Delta V) / (2m) \qquad\qquad (6)$$

Where C is the discharge capacitance, ΔV is the potential window of cycling, I is the discharge current and m is the mass of MnO_2.
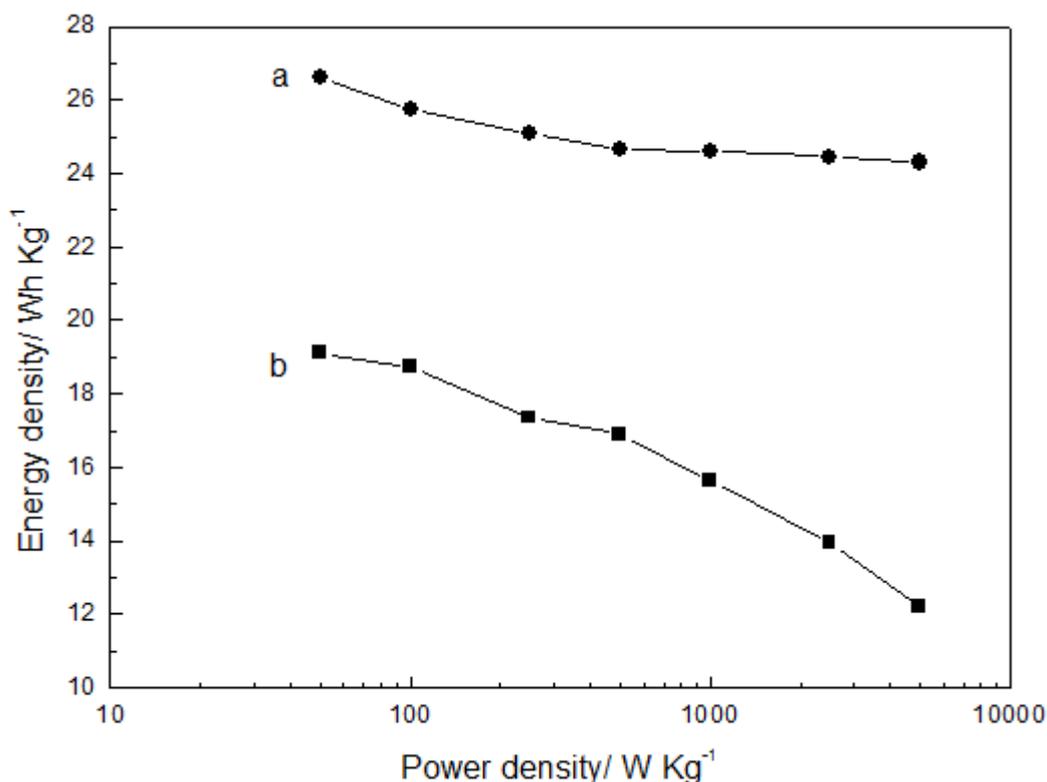
Figure 10. Ragone plots of the electrode J5(a) and J25(b).

It can be seen clearly that the electrode J5 has a much higher energy density than the electrode J25 and at the same time keeps a very high power density. For the electrode J5, having a 5mg cm^{-2} MnO$_2$ on the electrode, maximum energy density is 26.6 Wh Kg^{-1} at 50W Kg^{-1} and maintains 24.3 Wh Kg^{-1} at 5KW kg^{-1}, showing very good power-energy density properties. The electrode J25 has only an energy density of 19Wh Kg^{-1} at 50W Kg^{-1} and decreases to 12.2 Wh Kg^{-1} when the power density increases to 5KW Kg^{-1}. The good power-energy density characterization for the electrode J5 is due to its low resistance and fast ions diffusion process in MnO$_2$ phase.

4. CONCLUSIONS

Porous MnO$_2$ with a high specific surface area of 292m^2 g^{-1} and a high pore volume of 0.67cm^2 g^{-1} was prepared by a facial chemical route based on redox reaction between Mn^{2+} and MnO$_4^-$. The result of X-ray diffraction showed that the as-prepared MnO$_2$ was poor crystallization and amorphous. The electrochemical behavior of the as-prepared MnO$_2$ was investigated in a thin electrode (J5: MnO$_2$ mass=5mg cm^{-2}) and a thick electrode (J25: MnO$_2$ mass=25mg cm^{-2}), respectively. The CV curves and chronopotentiametry test showed that the both MnO$_2$ electrodes showed excellent pseudocapacitive behavior in the potential window of 0-1.0V. The SC of MnO$_2$ in the electrode J5 was much higher than that in the electrode J25 and kept high with the increasing of scan rates and current density due to the

lower electrochemical resistance and fast ion diffusion in the electrode J5. For a MnO_2 electrode with 5mg cm^{-2}, maximum energy density is 26.6 Wh Kg^{-1} at 50W Kg^{-1} and maintains 24.3Wh Kg^{-1} at 5KW Kg^{-1}, showing an excellent current capability. All the results proved that this porous MnO_2 can be used for applications in electrochemical supercapacitor.

References

1. B.E. Conway. Electrochemical Supercapacitors, Kluwer Academic Publishers, New York, 1999
2. Y. H. Wang, I. Zhitomirsky, *Langmuir* 25(2009) 9684.
3. A. Garcia-Gomez, P. Miles, T.A. Centeno, J.M. Rojo, *Electrochem. Solid State Letter* 13(2010) A112.
4. X.Y. Chen, H. Song, Z.J. Zhang, Y.Y. He, *Electrochimica Acta* 117(2014) 55
5. U.B. Nasini, V.G. Bairi, S.K. Ramasahayam, S.E. Bourdo, T. Viswanathan, A.U. Shaikh, *Journal Power Sources*, 250(2014) 257.
6. Y.Y. Horng, Y.C. Lu, Y.K.Hsu, C.C. Chen, L.C. Chen, K.H. Chen, *Journal of Power Sources* 195(2010) 4418.
7. J.T. Wei, S.S. Wei, G.B. Wang, X.P. He, B. Gao, C. Zhao, *European Polymer Journal*, 49(2013) 3651.
8. G.X. Hu, C.X. Li, H.Gong, *Journal Power Sources* 195(2010) 6977.
9. K. Karthikeyan, V. Aravindan, S.B. Lee, I.C. Jang, H.H. Lim, G.J. Park, M. Yoshio, Y.S. Lee, *Journal of Power Sources* 195(2010) 3761.
10. Y. Liu, W.W. Zhao, X.G. Zhang, *Electrochimica Acta* 53(2008) 3296.
11. T.Yousefi, A.N. Golikand, M.H. Mashhadizadeh, M. Aghazadeh, *Current Applied Physics* 12(2012) 193.
12. C.Y. Wan, M. Cheng, Q.S. Zhang, N.Q. Jia, *Powder Technology* 235 (2013) 706.
13. Y.H. Wang, H. Liu, X.L. Sun, I. Zhitomirsky, *Scripta Materialia* 61(2009) 1079.
14. H. Xia, J.K. Feng, H.L. Wang, M.O. Lai, L. Lu, *Journal of Power Sources* 195(2010) 4410.
15. C.L. Xu, Y.Q. Zhao, G.W. Yang, F.S. Li, H.L. Li, *Chemical Communication* 48(2009) 7575.
16. X.H. Tang, Z. H. Liu, C.X. Zhang, Z.P. Yang, Z.L. Wang, *Journal of Power Sources* 193(2009) 939.
17. S.H. Li, L. Qi, L.H. Lu, H.Y. Wang, *Journal of Solid State Chemistry* 197 (2013) 29.
18. P. Staiti, F. Lufrano, *Journal of Power Sources* 187(2009) 284.
19. C.Y. Wan, K. Azumi, H. Konno, *Electrochimica Acta* 52(2007) 3061.
20. L. Athouel, F. Moser, R. Dugas, O. Crosnier, D. Belanger, T. Brousse, *Journal of Physics Chemistry* C 112(2008) 7270.
21. M. Toupin, T. Brousse, D. Belanger, *Chemistry of Material* 16(2004) 3184.
22. O. A. Vargas; A. Caballero; L. Hernán; J. Morales. *Journal of Power Sources* 196(2011) 3350.
23. P. Ragupathy, H. N. Wasan, N. Munichandraiah, *Journal of the Electrochemical Society* 155(2008) A34.
24. M. W. Xu, D.D. Zhao, S. J. Bao, L.H. Li, *Journal of Solid State Electrochemisty* 11(2007) 1101.
25. J. Li, T.L. Que, J.B. Huang, *Materials Research Bulletin* 48 (2013) 747.
26. X.H. Yang, Y.G. Wang, H.M. Xiang, Y.Y. Xia, *Electrochimica Acta* 53(2007) 752.
27. R.R. Jiang, T. Huang, J.L. Liu, J.H. Zhang, A.S. Yu, *Electrochimica Acta* 54(2009)3047.
28. C.Y. Wan, L. Y. Wang, S.D. Shen, X. Zhu. *Acta Chimica Sinica* 67(2009) 1559.
29. N. Nagarajan, M. Cheong, I. Zhitomirsky, *Material Chemistry and Physics* 103(2007) 47.
30. K.R. Prasad, N. Miura, *Electrochemical Communication* 6(2004) 1004.
31. V. Srinivasan, J.W. Weidner, *Journal of the Electrochemical Society* 147(2000) 880.
32. M.W. Xu, L.B. Kong, W.J. Zhou, H.L. Li, *Journal of Physics Chemistry* C 111(2007) 19141.

33. S. Devaraj, N. Munichandraiah, *Journal of the Electrochemical Society* 154(2007) A80.
34. P. Sen, A. De, A.D. Chowdhury, S.K. Bandyopadhyay, N. Agnihotrib, M. Mukherjee, *Electrochimica Acta* 108(2013) 265.
35. J.H. Jang, A. Kato, K. Machida, K. Naoi, *Journal of the Electrochemical Society* 153(2006) A321.
36. S.C. Pang, M.A. Anderson, T.W. Chapman, *Journal of the Electrochemical Society* 147(2000) 444.